

Efficient Optimal Reconstruction of Linear Fields and Band-powers from Cosmological Data

B. Horowitz^{a,b} U. Seljak^{a,b} G. Aslanyan^a

^aBerkeley Center for Cosmological Physics and Department of Physics, University of California, Berkeley, CA 94720

^bLawrence Berkeley National Laboratory, Berkeley, CA 94720

E-mail: bhorowitz@berkeley.edu, useljak@berkeley.edu

Abstract. We present an efficient implementation of Wiener filtering of real-space linear field and optimal quadratic estimator of its power spectrum. By recasting the reconstruction into an optimization problem, we provide a flexible framework that can be used on a variety of cosmological fields. We present results for a variety of test cases, using simulated examples of projected density fields, projected shear maps from galaxy lensing, and observed Cosmic Microwave Background (CMB) temperature anisotropies, with a wide range of map incompleteness and variable noise. For smaller cases where direct numerical inversion is possible, we show that the maximum a posteriori solution matches that created by direct Wiener Filtering at a fraction of the overall computation cost. This technique allows for accurate map and power spectrum reconstruction even with complex masks and nontrivial noise properties.

Keywords: large scale structure – power spectrum, large scale structure – gravitational lensing, large scale structure – galaxy clusters

Contents

1	Introduction	1
2	Background	2
2.1	Likelihood Function for Bandpowers	3
2.2	Maximum Likelihood Field Reconstruction	3
2.3	Minimum Variance Estimation of the Power Spectra	4
2.3.1	Estimation of the Noise Bias and the Hessian	5
3	Example Cases	6
3.1	Projected Density Field	6
3.2	Cosmic Microwave Background Temperature	9
3.3	Cosmic Shear	10
4	Discussion and Conclusion	12
A	Wiener Filter Comparison	14
A.1	Review of Wiener Filtering	14
A.2	Wiener Filtering vs. MAP Projected Density Example	15
B	Convergence Criteria of CMB Reconstruction	17
C	Joint E & B Cosmic Shear Reconstruction	19

1 Introduction

A ubiquitous problem of modern astrophysics is the reconstruction of the underlying signal from observed, noisy, and incomplete data. For linear fields the Wiener filter [1, 2] is the gold standard for reconstructing the underlying signal, as it is “optimal” in the sense that it minimizes the variance. It has been used as the basis of cosmological analysis for both large scale structure [3, 4] and CMB [5, 6].

However, the Wiener filter requires one to take the inverse of the overall covariance matrix, which has a noise and a signal based components. Noise is typically diagonal in observed space, while signal is diagonal in harmonic (or Fourier) space. In general, the covariance matrix will not be diagonalizable in either basis and it will be computationally difficult to invert the matrix numerically for a realistic sized survey map. Workarounds to this problem have relied on making approximations, for example by assuming homogeneous and isotropic noise (as in, for example [7]), or requiring difficult to implement numerical schemes. Approximate matrix inversion techniques can be used, with recent works creating a messenger [8, 9] (or dual messenger [10]) field which can be diagonalized in either basis in which to run an approximation scheme. These methods have been argued to perform well versus other approximation schemes, but there are situations where the messenger field is zero (such as zero noise field with mask) and the method fails. In addition, it has been argued that a suitably chosen preconditioned conjugate gradient technique might be faster in some instances [11].

In this work we explore the efficient implementation of Wiener filter by using the well studied property that the Wiener filter is mathematically equivalent to maximum a posteriori (MAP), which in turn can be solved with fast linear algebra methods or optimization [12]. For cosmological analysis, it is not only the field that is of interest but also the band-powers (such as power spectrum amplitudes) and their covariance matrix. Work towards estimating these quantities jointly with the underlying field has been done in the cosmic shear context [9, 13], but it required sampling from the joint probability distribution which is computationally involved. In this work we examine ways to quickly compute these quantities for observations with complex noise and mask properties as well, and compare against those inferred from direct Wiener filtering.

In particular, we examine three cases of cosmological interest; linear density reconstruction, cosmic shear (E mode estimation alone as well as joint E/B), and primary CMB temperature anisotropy reconstruction. The outline of the paper is as follows: we discuss our maximum likelihood method for field and power spectrum estimation in §2. In §3, we use these tools in a number of contexts. In §4 we discuss our results and possible extensions of the work to analyze real data.

In Appendix A we review the critical results related to direct Wiener filtering which we compare our optimization method to for the small density field case. In Appendix B we discuss the convergence criteria in the case of primary CMB reconstruction. In Appendix C we discuss the joint estimation of E and B fields in the context of cosmic shear (although the technique transfers directly to CMB E and B reconstruction).

2 Background

Here we summarize the optimization technique and standardize notation. For a complete description, see [12, 14, 15].

We measure quantities $d(\mathbf{r}_i)$ at N positions, such as a reconstructed projected density, forming a full data vector, \mathbf{d} . In general, this data vector will depend on a combination of underlying information about the field (‘‘field coefficients’’) we wish to estimate, \mathbf{s} , and that which is pure noise, \mathbf{n} , i.e.

$$\mathbf{d} = \mathbf{R}\mathbf{s} + \mathbf{n}, \quad (2.1)$$

where the \mathbf{R} is the response matrix expressing how our measurement changes with the underlying information. We express the underlying Gaussian information in terms of covariance matrices, $\mathbf{S} = \langle \mathbf{s}\mathbf{s}^\dagger \rangle$, and $\mathbf{N} = \langle \mathbf{n}\mathbf{n}^\dagger \rangle$, for the estimated signal and noise components, respectively. We assume that these are uncorrelated with each other, i.e. $\langle \mathbf{n}\mathbf{s}^\dagger \rangle = 0$; changes to this assumption are tractable but would require a redefinition of our underlying likelihood function and complicate the analysis since the noise would carry signal information. The correlation matrix of the data is therefore,

$$\begin{aligned} \langle \mathbf{d}\mathbf{d}^\dagger \rangle \equiv \mathbf{C} &= \langle (\mathbf{R}\mathbf{s} + \mathbf{n})(\mathbf{R}\mathbf{s} + \mathbf{n})^\dagger \rangle \\ &= \langle (\mathbf{R}\mathbf{s}(\mathbf{R}\mathbf{s})^\dagger + \mathbf{n}\mathbf{n}^\dagger + \text{Cross Terms}) \rangle \\ &= \mathbf{R}\mathbf{S}\mathbf{R}^\dagger + \mathbf{N}. \end{aligned} \quad (2.2)$$

Our signal covariance, \mathbf{S} , takes a diagonal form in Fourier space. The noise covariance, \mathbf{N} , is approximately diagonal in real space, as there usually are no noise correlations between pixels. This will lead to very strong off-diagonal terms in Fourier space in the presence of masked sky regions and/or variable noise properties. Therefore, our overall data correlation matrix cannot be diagonalized easily in either basis.

2.1 Likelihood Function for Bandpowers

We now want to find the most probable set of bandpowers, Θ , for a given set of measurements \mathbf{d} . We thus parametrize the power spectrum as a function of these bandpowers $\mathbf{S}(\Theta)$. If we assume our modes are Gaussian we can express the likelihood function in the familiar form, i.e.

$$L(\mathbf{d}|\Theta) = (2\pi)^{-N/2} \det(\mathbf{C})^{-1/2} \exp\left(-\frac{1}{2}\mathbf{d}^\dagger \mathbf{C}^{-1} \mathbf{d}\right). \quad (2.3)$$

Associated with the likelihood function and a parameter set $\hat{\Theta}$ which maximizes it, is the Hessian matrix [16],

$$F_{ll'} = -\frac{\partial^2 \ln L}{\partial \Theta_l \partial \Theta_{l'}}. \quad (2.4)$$

The inverse of the Hessian matrix can be interpreted as an estimate of the covariance matrix of the parameters, i.e.

$$\mathbf{F}^{-1} = \langle \Theta \Theta^\dagger \rangle - \langle \Theta \rangle \langle \Theta \rangle^\dagger. \quad (2.5)$$

Using Newton's second order method we can create a quadratic estimator of the form [17]

$$\Theta_l = \frac{1}{2} \sum_{l'} F_{ll'}^{-1} (\mathbf{d}^\dagger \mathbf{C}^{-1} \mathbf{Q}_{l'} \mathbf{C}^{-1} \mathbf{d} - b_{l'}), \quad (2.6)$$

where b is a noise bias term that can be found by computing the ensemble average of the first term assuming $\theta_l = 0$ for all modes probed (i.e. $l < l_{\max}$),

$$b_l = \text{tr} \left[\mathbf{N} + \sum_{l_{\max}+1}^{\infty} (\Theta_l \mathbf{Q}_l) \mathbf{C}^{-1} \mathbf{Q}_l \mathbf{C}^{-1} \right]. \quad (2.7)$$

2.2 Maximum Likelihood Field Reconstruction

In practice this analytical calculation requires the inversion of a large matrix, \mathbf{C} , which does not necessarily have properties that make inversion efficient (i.e. block diagonal or sparse) and will in general require $O(n^3)$ time for an $n \times n$ matrix. In the case of reconstructing the underlying density field for astronomical large surveys with n pixels, this would be prohibitively computationally expensive for the foreseeable future. Instead, we will approach this as an optimization problem using an L-BFGS optimizer. To begin this process we return to the likelihood expression in Equation 2.3, but instead of expressing the likelihood of data given bandpowers we will work in terms of likelihood of underlying modes \mathbf{s} given the data,

$$L(\mathbf{s}|\mathbf{d}) = (2\pi)^{-(N+M)/2} \det(\mathbf{S}\mathbf{N})^{-1/2} \exp\left(-\frac{1}{2}\mathbf{s}^\dagger \mathbf{S}^{-1} \mathbf{s} + (\mathbf{d} - \mathbf{R}\mathbf{s})^\dagger \mathbf{N}^{-1} (\mathbf{d} - \mathbf{R}\mathbf{s})\right), \quad (2.8)$$

and note that the minimum variance solution for the modes can be found by minimizing the loss function χ^2 ,

$$\chi^2 = \mathbf{s}^\dagger \mathbf{S}^{-1} \mathbf{s} + (\mathbf{d} - \mathbf{R}\mathbf{s})^\dagger \mathbf{N}^{-1} (\mathbf{d} - \mathbf{R}\mathbf{s}), \quad (2.9)$$

with respect to \mathbf{s} . Expanding this to quadratic order around some fixed \mathbf{s}_m we have

$$\chi^2 = \chi_0^2 + 2\mathbf{g}(\mathbf{s} - \mathbf{s}_m) + (\mathbf{s} - \mathbf{s}_m) \mathbf{D} (\mathbf{s} - \mathbf{s}_m), \quad (2.10)$$

with gradient function

$$\mathbf{g} = \frac{1}{2} \frac{\partial \chi^2}{\partial \mathbf{s}} = \mathbf{S}^{-1} \mathbf{s}_m - \mathbf{R}^\dagger \mathbf{s}_m \mathbf{N}^{-1} (\mathbf{d} - \mathbf{R} \mathbf{s}_m). \quad (2.11)$$

For the linear problems studied in this work, this derivative can be calculated analytically, but in other more involved cases (such as nonlinear structure formation) might be computationally involved as it would require intensive back-propagation. The solution where $\mathbf{g} = 0$, and therefore a local extremum is found, will be denoted $\hat{\mathbf{s}}$, and is the maximum a posteriori solution (MAP). For linear problems it is the best possible solution in the sense to minimizing the variance.

The curvature matrix \mathbf{D} can be calculated numerically at each step, or built up iteratively (like in the BFGS approach), and has the form

$$\mathbf{D} = \frac{1}{2} \frac{\partial^2 \chi^2}{\partial \mathbf{s} \partial \mathbf{s}} = \mathbf{S}^{-1} + \mathbf{R}^\dagger \mathbf{N}^{-1} \mathbf{R}. \quad (2.12)$$

The starting point for the optimization algorithm does not play a significant role for linear problems as the likelihood surface is convex and the true global minimum can always be found. In practice, for the cases in this work, we found no noticeable effects of the starting point in terms of convergence properties, i.e. required number of iterations.

2.3 Minimum Variance Estimation of the Power Spectra

The result of the optimization procedure, $\hat{\mathbf{s}}$, described above is useful for creating maps, but has more information than needed for cosmological analysis. If our goal is to determine a set of summary statistics/band-power measurement, Θ , such as a power spectrum bandpowers, we need to marginalize over latent variables, the modes \mathbf{s} . To do so we need to define a projection matrix Π_l around a fiducial power-spectrum \mathbf{S}^{fid} defined as

$$\left[\frac{\partial \mathbf{S}}{\partial \Theta_l} \right]_{\mathbf{S}^{\text{fid}}} = \Pi_l. \quad (2.13)$$

The true covariance can be written in terms of this fiducial power-spectrum plus a term linear in the projection operators:

$$\mathbf{S} = \mathbf{S}^{\text{fid}} + \sum_l \Delta \Theta_l \Pi_l. \quad (2.14)$$

For the cases studied in this work, the dependence of \mathbf{S} on Θ is linear so we can take

$$\Pi_l = \frac{\mathbf{S}^{\text{fid}}}{\Theta_l}, \quad (2.15)$$

i.e. the projection matrix takes the power spectrum per bin, Θ_l , to the full power spectrum, \mathbf{S} . Note that the choice of the fiducial model is important in that if it is sufficiently far away from the true model the result could be biased, but iteratively recalculating \mathbf{S}^{fid} with the solved new band-powers adjusted by $\Delta \Theta$ will provide an asymptotically more accurate reconstruction. In the cases of interest in this work, no iterative process was necessary to provide an accurate reconstruction.

To compute the posterior distribution of band-powers we can write the likelihood function to maximize as a second order expansion around the fiducial model

$$\ln L(\Theta_{\text{fid}} + \Delta \Theta) = \ln L(\Theta_{\text{fid}}) + \sum_l \left[\frac{\partial \ln L(\Theta)}{\partial \Theta_l} \right]_{\Theta_{\text{fid}}} \Delta \Theta_l + \frac{1}{2} \sum_{l'l'} \left[\frac{\partial^2 \ln L(\Theta)}{\partial \Theta_l \partial \Theta_{l'}} \right]_{\Theta_{\text{fid}}} \Delta \Theta_l \Delta \Theta_{l'}; \quad (2.16)$$

where we assume a flat prior on the band-powers. To compute the derivative terms we need to take the derivatives of terms in Eq. 2.8. Analytically these can be defined as

$$\frac{\partial [(d - \mathbf{R}\hat{\mathbf{s}})^\dagger \mathbf{N}^{-1}(d - \mathbf{R}\hat{\mathbf{s}})]}{\partial \Theta_l} = -2 \left[\mathbf{R} \frac{\partial \hat{\mathbf{s}}}{\partial \Theta_l} \right]^\dagger \mathbf{N}^{-1}(d - \mathbf{R}\hat{\mathbf{s}}) = -2 \left[\frac{\partial \hat{\mathbf{s}}}{\partial \Theta_l} \right]^\dagger \mathbf{S}_{\text{fid}}^{-1} \hat{\mathbf{s}} \quad (2.17)$$

and

$$\frac{\partial [\hat{\mathbf{s}}^\dagger \mathbf{S}_{\text{fid}}^{-1} \hat{\mathbf{s}}]}{\partial \Theta_l} = 2 \left[\frac{\partial \hat{\mathbf{s}}}{\partial \Theta_l} \right]^\dagger \mathbf{S}_{\text{fid}}^{-1} \hat{\mathbf{s}} - 2E_l(\mathbf{S}_{\text{fid}}, \hat{\mathbf{s}}), \quad (2.18)$$

defining

$$E_l(\mathbf{S}_{\text{fid}}, \hat{\mathbf{s}}) = \frac{1}{2} \hat{\mathbf{s}}^\dagger \mathbf{S}_{\text{fid}}^{-1} \mathbf{\Pi}_l \mathbf{S}_{\text{fid}}^{-1} \hat{\mathbf{s}} = \frac{1}{2} \sum_{k_l} \frac{\hat{s}_{k_l}^2}{\Theta_{\text{fid},l} S_{\text{fid},k_l}}, \quad (2.19)$$

where in the last equality we made use of the diagonal property of the projection operators and fiducial power spectrum. Putting this together we find that the derivative of the likelihood can be expressed as

$$\frac{\partial \ln L(\boldsymbol{\Theta})}{\partial \Theta_l} = E_l - b_l, \quad (2.20)$$

where we defined

$$b_l = \frac{1}{2} \text{tr} \left[\frac{\partial \ln(\mathbf{S}\mathbf{N}\tilde{\mathbf{D}})}{\partial \Theta_l} \right]_{\mathbf{S}_{\text{fid}}}. \quad (2.21)$$

For the linear cases studied in this work, this term is often called the noise bias term, because if we start from $\mathbf{S} = 0$ the noise is the only source of this term. However, it is worth remembering that this term's origin is the derivative of the log determinant of the product of the Hessian and the signal covariance matrices in equation 2.21 (since noise covariance derivative is zero). To find the most likely point we need to find the zero of Eq. 2.20, which we solve using Newton's method. To do this we define the Hessian matrix,

$$F_{ll'} = - \frac{\partial^2 \ln L(\boldsymbol{\Theta})}{\partial \Theta_l \partial \Theta_{l'}}, \quad (2.22)$$

which for linear models defines exactly the Gaussian posterior assuming sufficient modes have been sampled. The peak of the likelihood function can be found by setting the derivative of equation 2.16 with respect to $\boldsymbol{\Delta}\boldsymbol{\Theta}$ to zero, which upon inserting equation 2.20 yields

$$(\mathbf{F}\boldsymbol{\Delta}\hat{\boldsymbol{\Theta}})_l = E_l - b_l. \quad (2.23)$$

2.3.1 Estimation of the Noise Bias and the Hessian

While the noise bias, b_l , and the Hessian matrix, \mathbf{F} , from Equation 2.23 could be calculated exactly, this will involve inversion of large matrices, which is what we are trying to avoid by deriving the MAP via optimization techniques. Instead, we will perform a simulation based analysis motivated by the underlying definition of each of these terms.

In general, the maximum likelihood field, $\hat{\mathbf{s}}$, attained with the procedure described in Sec 2.2, will have bias due to the presence of noise: when the noise is high the minimum variance estimator drives \mathbf{s} to zero. In the case of cosmological density fields which have red power spectra (less power on small scales compared to white noise), this will result in washing out the small scale power. See the figures in Sec 3 for explicit examples.

To correct for this bias we need to understand how our reconstruction responds to the presence of noise. For this we perform a simulation analysis wherein we generate a data realization generated from a fiducial power spectrum, inject the noise and mask, perform the optimization and see how the presence of noise affects the reconstruction. Let us call the new data and noise realization data \mathbf{d}_{s+n} , with associated maximum likelihood reconstruction $\hat{\mathbf{s}}_{s+n}$. The gradient of equation 2.20 has to vanish if evaluated at the fiducial model. The noise bias in this case can be found directly as

$$b_l = E_l(\Theta_{\text{fid}}, \hat{\mathbf{s}}_{s+n}). \quad (2.24)$$

This quantity should be averaged over many realizations, but for the linear signal-dominated cases studied in this work we found even one realization was sufficient for an accurate reconstruction.

To calculate the Hessian matrix, we evaluate the gradient of equation 2.20 at two different fiducial model values, and use finite differentiation,

$$F_{ll'} \Delta\Theta_{l'} = E_l(\Theta_{\text{fid}} + \Delta\Theta_{l'}) - b_l(\Theta_{\text{fid}} + \Delta\Theta_{l'}) - E_l(\Theta_{\text{fid}}) + b_l(\Theta_{\text{fid}}). \quad (2.25)$$

This can be further simplified for linear models, as discussed in [15].

3 Example Cases

Here we implement the above scheme in a number of simulated cosmological contexts to demonstrate its versatility and efficiency. For these cases, we set our convergence criteria to be $\epsilon \equiv \delta\chi^2 = 10^{-1}$; i.e. the optimization ends when the difference of the absolute chi-square values between iterations is 10^{-1} . In Appendix B we discuss the choice of this criteria in the context of CMB reconstruction, but we have found it to be sufficient for all the example cases.

3.1 Projected Density Field

As our first case, we will look at reconstructing the density field from a noisy measurement of said density field. The starting measurement could come from a variety of observations such as galaxy clustering or Lyman alpha forest tomography. For a complete analysis one would specify the response matrix \mathbf{R} to go from the density to the observables which would include a model for the various biases present in the observations. In this case we assume the bias model is known and deal directly with the matter density field.

We generate a Gaussian random field with a power-spectrum given by

$$P(k) \propto \frac{k}{1 + k^3} \quad (3.1)$$

over a 2D, $L = 1380$ Mpc/h side-length box. We introduce an anisotropic white noise over the field to simulate either irregularities in depth of a given survey or theoretical uncertainties in the underlying bias model. In Appendix A we demonstrate the validity of the L-BFGS optimization method in a small test case (64×64 pixel) where it is also tractable to exactly invert the full covariance matrix numerically thereby providing validation of our maximum likelihood technique, while here we examine a more realistic 512×512 pixel map. We also use a realistic mask which includes foreground stars and other potential image defects.

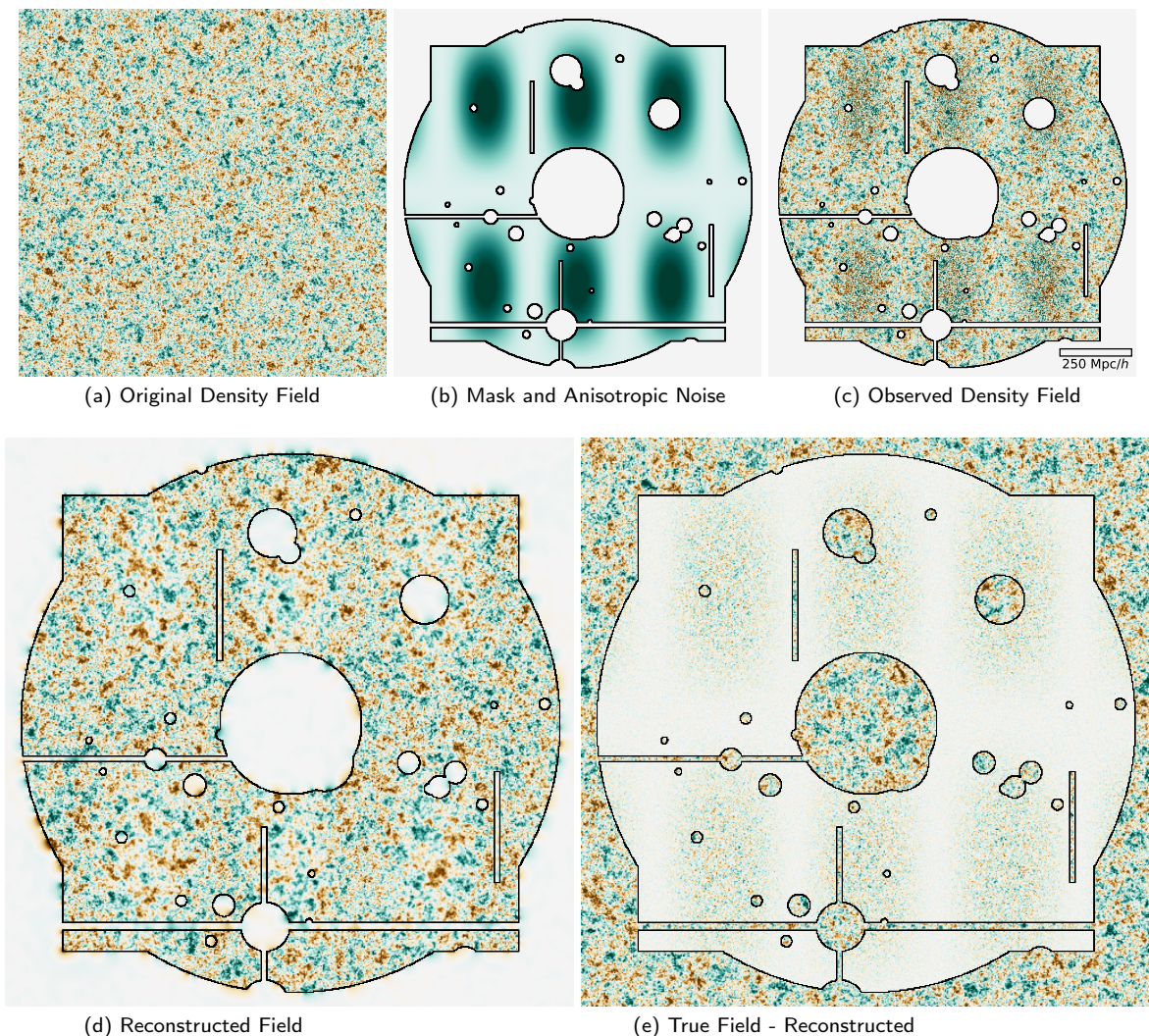


Figure 1: MAP density reconstruction for the 512x512 pixel case. Note that images (a), (c), (d), and (e) have the same absolute color scale, while (b) shows the spatial variance of the noise properties.

Using the input power spectrum of Eq. 3.1, we generate a density field shown in Fig 1(a), apply a mask and anisotropic noise shown in Fig 1(b), which results in a mock observation in Fig 1(c). We perform the minimization routine outlined in Sec. 2.2, with the optimized map shown in Fig. 1(d) with residuals shown in Fig 1(e). Qualitatively, the reconstructed field does an excellent job within the mask in the low-noise regions and is even able to reconstruct the larger scale modes right on the border within the masked region. However, as expected, the small scale modes within the high noise regions within the mask are poorly reconstructed since it is impossible to differentiate those modes in real space with the noise. In addition, small masked regions have very low residual error as there are sufficient, well sampled, nearby large scale modes to infer the regions value.

In Fig 2 we show the comparison of the optimized result with the true power-spectra of the entire field. We also show the effect of the noise bias correction, which in this case is

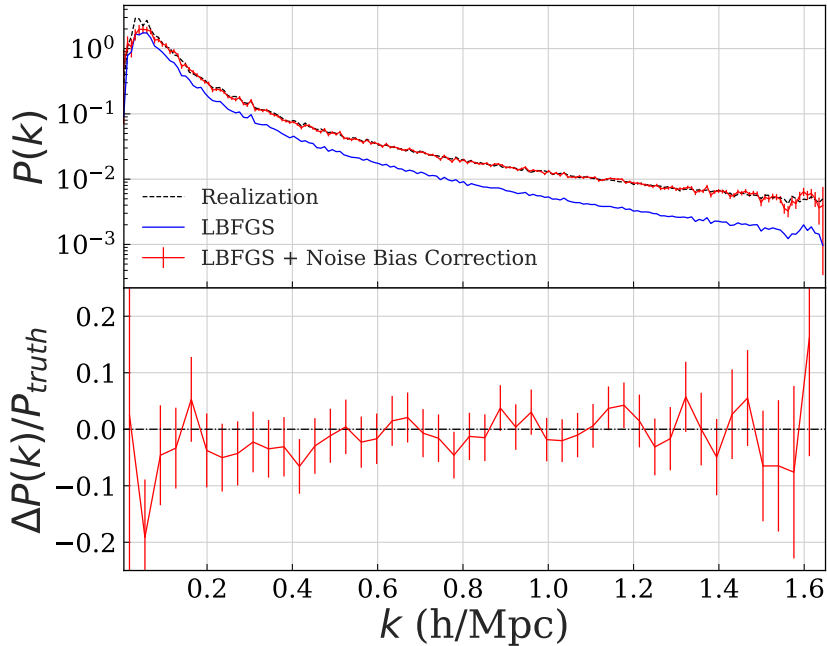


Figure 2: Comparison of the maximum likelihood power spectrum attained from optimization versus the true power-spectrum of the region. Also shown is the importance of the noise bias correction (or, equivalently, the importance of the Hessian determinant).

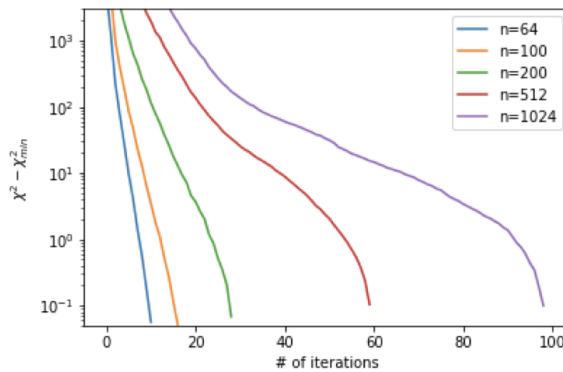


Figure 3: Convergence properties of the L-BFGS estimator as a function of the box-side dimension n .

substantial as small scale power is washed out in the high noise regions as well as due to the masked regions. However, this power is recoverable using the analysis described in Section 2.

In Fig 3 we show how the number of iterations of the reconstruction algorithm scales with the box size. Each iteration requires a calculation of the cross function and the derivatives of the field which can be found analytically. Notice that the iteration number increases with

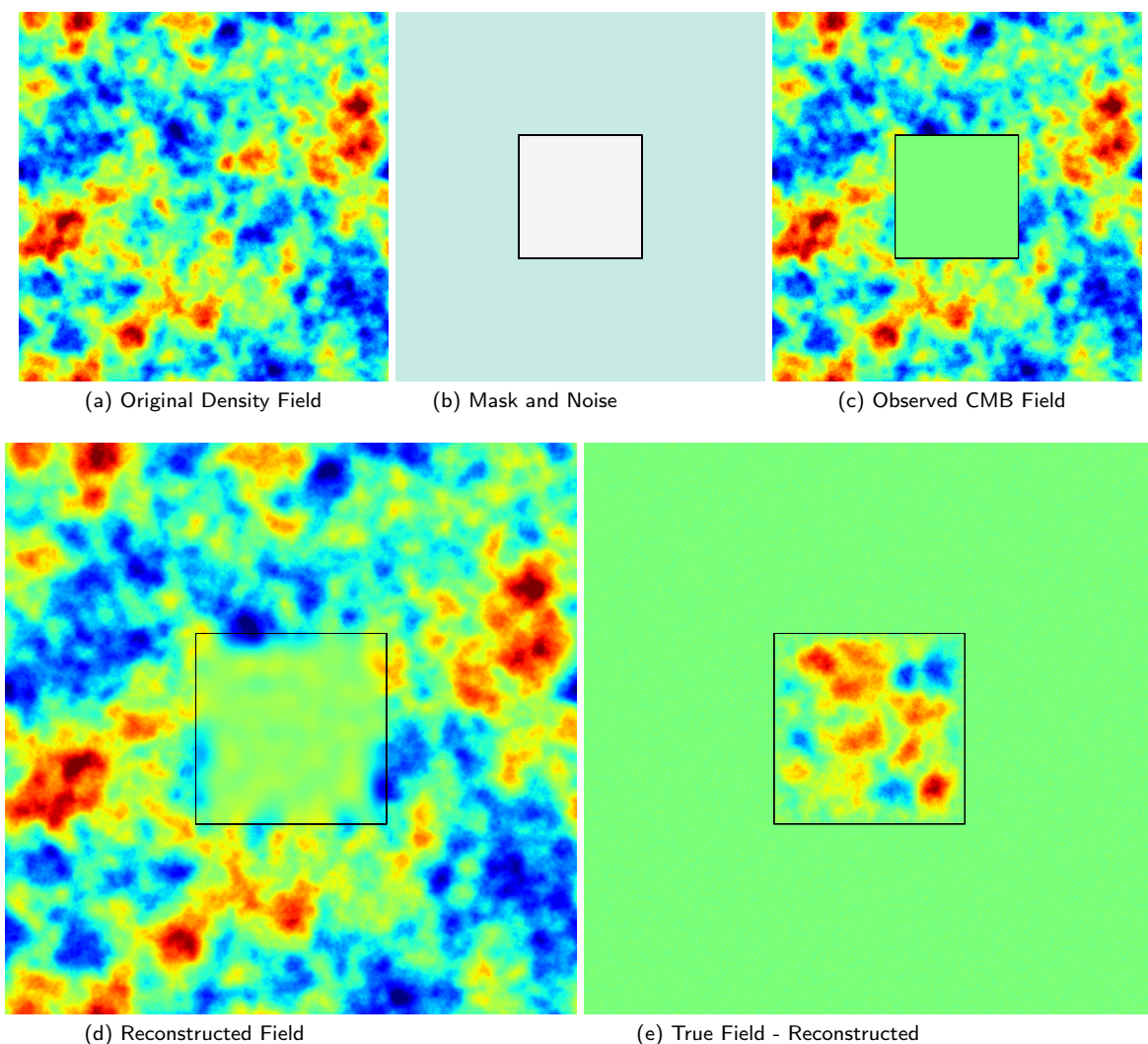


Figure 4: MAP CMB reconstruction for 512x512 pixel map.

the box size, but only a factor of a few when going from 64^2 to 1024^2 . This does not include estimation of the noise bias and the Hessian matrix, which will depend on the number of bandpowers. As each row of the Hessian matrix requires an additional optimization, the true number of iteration will scale linearly with the number of bandpowers. In practice, since the Hessian matrix is very smooth and nearly translationally invariant (in this case, it is peaked on the diagonal and monotonically decreasing away from the diagonal), one simply needs to sample the matrix along a small number of rows and interpolate between them.

3.2 Cosmic Microwave Background Temperature

The question of optimal reconstruction of CMB maps given irregular sky coverage and variable noise and foreground subtraction is a common issue for existing CMB surveys. So far, true maximum likelihood estimators have only been applied to data from WMAP [6] and on the largest angular scales in Planck data [18], but these techniques are difficult to scale to the entire Planck dataset due to the significant increase in computational cost.

While Planck’s power spectrum measurements, and therefore cosmological parameter constraints [19], do not rely on construction of the actual full map, other spatially dependent signals do. Cross-correlations between the primary CMB and other cosmological probes, such as x-ray signal or galaxy positions, require an accurate spatial reconstruction of the CMB map. In addition, full sky CMB lensing maps are constructed by applying the quadratic estimators to the CMB map (in either temperature, polarization, or some minimum variance combination of the two) and will similarly suffer if the reconstructed temperature and/or polarization maps are suboptimal.

In Figure 4 we show results for temperature, without polarization. We mention that polarization would be analogous to the example of joint optimization of E and B fields, which we do in the case of cosmic shear in Appendix C.

The case of CMB reconstruction is analogous to that of the density field, but with a significantly redder spectrum. The condition number of the covariance matrix is thus significantly larger, and BFGS needs more iterations to converge. While we could have used conjugate gradient with a preconditioner to improve the convergence of the optimization step, we chose not to do so here since the computational cost was not significantly higher even for this case (figure 6). For the implementation of our algorithm it is important to recognize that the increase in power on larger scales in the CMB case makes the masked region the most computationally expensive region to reconstruct, and a redder spectrum will allow more mode reconstruction within this region.

We generate a mock primary CMB full-sky field using HEALPIX [20] based on power spectrum generated from CLASS using the Planck 2015 cosmological parameters [19]. We then extract a 10×10 degree patch which we then mask a central region and introduce a white noise of $6 \mu K$ -arcmin.

The reconstruction is quite good in the observed region as the presence of noise mostly affects small scales where there is very little power. In the masked region the optimization is able to reproduce some clear long-scale modes. In Appendix B we show that with a more accurate convergence criteria we reproduce more of these large scale modes in the masked region but in terms of power spectrum estimation this is unnecessary, as we are already cosmic variance limited even with $\epsilon = 0.1$.

3.3 Cosmic Shear

Here we briefly summarize the theoretical foundations of cosmic shear as a tool to probe the matter power spectra. For a more complete survey of cosmic shear see [21–23]. For this section we specialize to only fitting a curl-free E component; we discuss the more general case including a curl component in Appendix C.

We want to relate the projected density field to the deformed images of galaxies in a given survey. Let us take a survey of N galaxies located at angular position θ_i , each with an associated two-component vector $\{e_1, e_2\} = \{e \cos 2\phi, e \sin 2\phi\}$ where e is the ellipticity and ϕ is the angle of the major axis. The gravitational lensing distorts the true surface brightness to an observed surface brightness by a deflection angle $\delta\theta$, i.e. $I_{\text{obs}}(\theta) = I_{\text{true}}(\theta + \delta\theta)$. The correlations between nearby galaxies is expressed in the symmetric deformation tensor,

$$\Phi_{ij} = \frac{\partial(\delta\theta_i)}{\partial\theta_j} = -2 \int_0^{\chi_0} g(\chi) \nabla_i \nabla_j \phi(\chi) d\chi, \quad (3.2)$$

where χ is the comoving distance, χ_0 is the horizon distance, and the lensing kernel, $g(\chi)$, depends on the normalized distribution of galaxies, $W(\chi)$, in a flat universe as

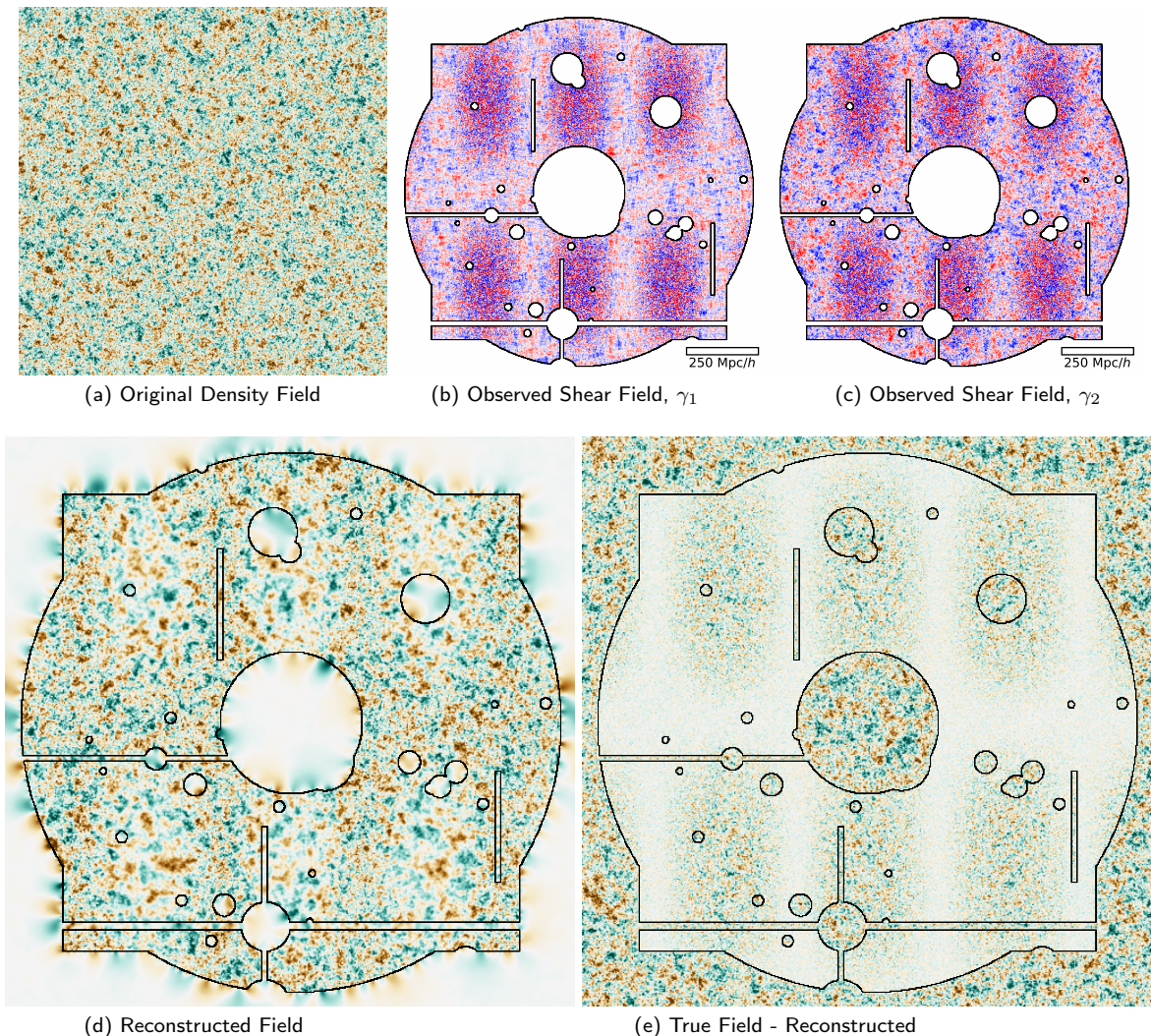


Figure 5: Maximum likelihood shear reconstruction for a 512x512 pixel map. Here we use the same mask and noise properties as shown in Figure 1.

$$g(\chi) = \chi \int_{\chi}^{\chi_0} \frac{\chi' - \chi}{\chi} W(\chi') d\chi'. \quad (3.3)$$

We can now decompose the deformation tensor into its trace component, the convergence κ , and two trace-free components, the shear γ_1 and γ_2 , as

$$\Phi_{ij} = \begin{bmatrix} 1 - \kappa - \gamma_1 & -\gamma_2 \\ -\gamma_2 & 1 - \kappa + \gamma_1 \end{bmatrix}. \quad (3.4)$$

With this deformation matrix in mind we can relate the ellipticity change to the convergence and shear by $e_i = \gamma_i / (1 - \kappa)$. However, in the case of large scale structure away from massive clusters we are in the weak lensing regime where $\kappa \ll 1$, so we can safely drop convergence terms which allows us to directly relate the shear with the observed ellipticity of galaxies, $e_i = \gamma_i$, and we do not need to worry about potential singular behavior of the

deformation matrix (where $|\det\Phi| = 0$). Binning these galaxies, we can create two shear fields, one for each shear component.

To apply our method, we perform optimization over this underlying density field and at each step of the optimization compute the corresponding shear maps, γ_1 and γ_2 , to compare with the observed shear maps. In principle, instead of working with the shear maps which require binning and/or interpolation between galaxies, one could work directly with the catalog of galaxy shapes and compute the likelihood of the observed ellipticity instead of the given averaged shear maps (as in [24, 25]).

This method is in contrast to the standard Kaiser-Squires (KS) [26] technique which has proven quite successful so far in cosmic shear analysis and cluster mass estimation. However, KS has some notable downsides in the presence of anisotropic noise or a mask as it is not able to self consistently down-weight the high noise areas and masked regions, resulting in defects on boundaries. In addition, the noise inherent in these measurements propagates onto the final mass-maps, resulting in an inaccurate small scale power measurement. This has been shown to be particularly detrimental to peak statistics measurements [27].

The results in position space are shown in Figure 5. In Figure 5(a) we show the initial density field and in Figure 5(b,c) we show the observed shear fields including mask and noise properties. Our reconstructed maximum likelihood map is shown in Figure 5(d) and the difference between the original field and reconstructed in Figure 5(e). As in the case of the density field, the optimization technique is able to exactly reconstruct the density in the low noise, unmasked regions, but only recovers large scale power in the higher noise unmasked regions.

4 Discussion and Conclusion

In this work we have demonstrated that it is possible to efficiently reconstruct the signal field and the maximum likelihood power spectrum for linear fields for realistic survey sizes. This technique is equivalent to the Wiener filter solution for small enough convergence criteria and has been applied to a number of cosmological fields (density, CMB, and cosmic shear maps). We are able to reconstruct the initial density field and the overall power spectrum, accounting for noise bias and window-function effects due to masking.

This technique outperforms the brute force Wiener filter technique in terms of computational time and memory requirements. True Wiener filter requires an inversion of the full pixel covariance matrix, \mathbf{C} , which for realistic surveys would be highly non trivial. Our technique avoids this issue by recasting the problem into an optimization scheme. This allows us to use off the shelf optimization codes such as L-BFGS, as well as convergence criteria to find the proper trade-off point between accuracy and computation time. We compare the two in Appendix A, finding good agreement for low dimensionality problems where brute force approach is feasible.

In Figure 6 we show the convergence properties for the 3 cases studied in Section 3, as well as the joint E/B cosmic shear case presented in Appendix C. While all the cases have a comparable number of unmasked pixels, convergence properties differ due to the difference of the underlying fields power-spectrum. More power at larger scales (i.e. a redder spectra) requires additional iterations to reconstruct the power within the masked regions.

While we used L-BFGS due to its well established optimization properties in very high dimensional convex optimization problems, we do not make a claim of optimality in terms of the particular technique for performing the optimization. As we examined primarily linear

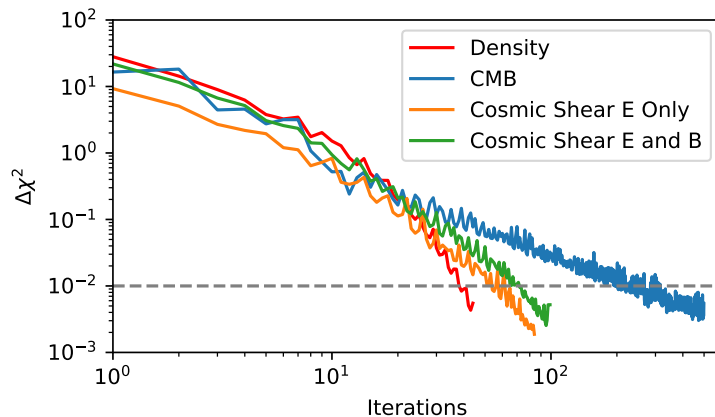


Figure 6: Comparison of the convergence properties of the various cosmological density fields studied in this work. All cases have 512^2 pixels, and comparable effective volume.

fields, L-BFGS was particularly useful as the iteratively constructed low rank Hessian approximation makes it quasi-Newton. Since linear problems are convex, an optimizer is guaranteed to find the global minimum. In general, we did not find particularly large performance changes when using other optimization techniques, such as conjugate gradient. Sampling based methods, like Hamiltonian Monte Carlo, are unnecessary for these linear cases, as there is no need to sample the distribution which is well approximated as a multivariate Gaussian.

A comparison can be made in our primary CMB example in Section 3.2 to the results of the messenger and dual messenger field found in [10] (see Figure 6 in [10]). The L-BFGS approach requires significantly fewer iterations than the messenger field ($\sim 5x$) and dual messenger field ($\sim 2x$) for a comparable convergence criteria. It is possible that an optimized cooling scheme for the messenger/dual messenger field would yield similar convergence properties, but this choice would likely be problem-specific and introduce an additional parameter to tune in the optimization. In general we see little benefit in using these specialized methods over the off the shelf standard optimization methods.

Going forward, it will be useful to extend this technique to other cosmological observables such as cosmic shear tomography (such as in [14]), Lyman - α tomography, and CMB lensing. Already work has been done applying this maximum likelihood approach to CMB lensing [28, 29], and further extending this work with these methods to small scales where standard quadratic estimators [30] are known to be suboptimal [31] would be promising future approach. Another avenue of particular interest is the ability for this technique to be useful for combining multiple (biased) tracers of some underlying field to create a maximum likelihood estimate of the field. One particularly promising example is jointly maximizing the underlying density likelihood function with respect to both the shear map as well as the projected galaxy density map [32, 33].

Acknowledgments

We would like to thank Vanessa Böhm, Simone Ferraro, Stephanie Ger, Chirag Modi, and Michael Schneider for useful discussions and/or comments during the preparation of this

manuscript. BH is supported by the NSF Graduate Research Fellowship, award number DGE 1106400. US acknowledges support from NSF 1814370, NSF 1839217, NASA 17-ATP17-0007 and NNX15AL17G.

This research has made use of NASA’s Astrophysics Data System. This research used resources of the National Energy Research Scientific Computing Center, a DOE Office of Science User Facility supported by the Office of Science of the U.S. Department of Energy under Contract No. DE-AC02-05CH11231.

A Wiener Filter Comparison

To demonstrate the optimality of our method we compare directly against the well established Wiener filter method.

A.1 Review of Wiener Filtering

Wiener filtering (WF) [1, 2] is a popular way to non-parametrically reconstruct cosmological data as, in the linear case, it should minimize variance. In the absence of non-Gaussian sources of signal or noise, WF is optimal in the sense that it is equal to the maximum posterior probability estimator [15]. Here we want to reconstruct the field itself, \mathbf{s} , given the noisy and/or poorly sampled data, \mathbf{d} . We define our estimated field $\hat{\mathbf{s}} = \Phi \mathbf{d}$, where Φ is a linear operator, i.e. a $N \times M$ dimensional matrix transforming from “image space” to “field space”. This can be found by attempting to minimize the variance of the residual

$$\langle (\mathbf{s} - \hat{\mathbf{s}})(\mathbf{s} - \hat{\mathbf{s}})^\dagger \rangle \quad (\text{A.1})$$

with respect to Φ . The Wiener filtered estimator is

$$\hat{\mathbf{s}} = \Phi \mathbf{d} = \langle \mathbf{s} \mathbf{d}^\dagger \rangle \langle \mathbf{d} \mathbf{d}^\dagger \rangle^{-1} \mathbf{d} = \mathbf{S} \mathbf{R}^\dagger \mathbf{C}^{-1} \mathbf{d}, \quad (\text{A.2})$$

which will result in a variance of residuals of the form

$$\langle (\mathbf{s} - \hat{\mathbf{s}})(\mathbf{s} - \hat{\mathbf{s}})^\dagger \rangle = \mathbf{S} - \mathbf{S} \mathbf{R}^\dagger \mathbf{C}^{-1} \mathbf{R} \mathbf{S}. \quad (\text{A.3})$$

Wiener filter only uses the mean and variance of the statistical distribution. If our underlying field is strongly non-Gaussian the WF may no longer be optimal. However, it will still minimize the variance, as defined in equation 2.5, just that this minimization of variance may not correspond to the notion of the best reconstruction. It may be difficult to even define a measure to use for optimality of reconstruction in these cases, although nonlinear reconstruction methods certainly exist [15].

We now want to connect the Wiener Filter solution to the optimal power spectrum estimator. We multiply equation 2.6 by the Hessian matrix,

$$\begin{aligned} (\mathbf{F}\Theta)_l &= \frac{\mathbf{F}}{2} \sum_{l'} F_{ll'}^{-1} (\mathbf{d}^\dagger \mathbf{C}^{-1} \mathbf{Q}_{l'} \mathbf{C}^{-1} \mathbf{d} - b_{l'}), \\ &= \frac{\delta_{ll'}}{2} (\mathbf{d}^\dagger \mathbf{C}^{-1} \mathbf{\Pi}_{l'} \mathbf{R} \mathbf{R}^\dagger \mathbf{\Pi}_{l'} \mathbf{C}^{-1} \mathbf{d} - b_{l'}), \\ &= \frac{1}{2} ((\mathbf{\Pi}_l \mathbf{R}^\dagger \mathbf{C}^{-1} \mathbf{d}) (\mathbf{\Pi}_l \mathbf{R}^\dagger \mathbf{C}^{-1} \mathbf{d})^\dagger - b_l). \end{aligned} \quad (\text{A.4})$$

The noise \mathbf{b} can be similarly transformed as

$$b_l = \text{tr}(\mathbf{\Pi}_l \mathbf{R}^\dagger \mathbf{C}^{-1} (\mathbf{N}) \mathbf{C}^{-1} \mathbf{R} \mathbf{\Pi}_l), \quad (\text{A.5})$$

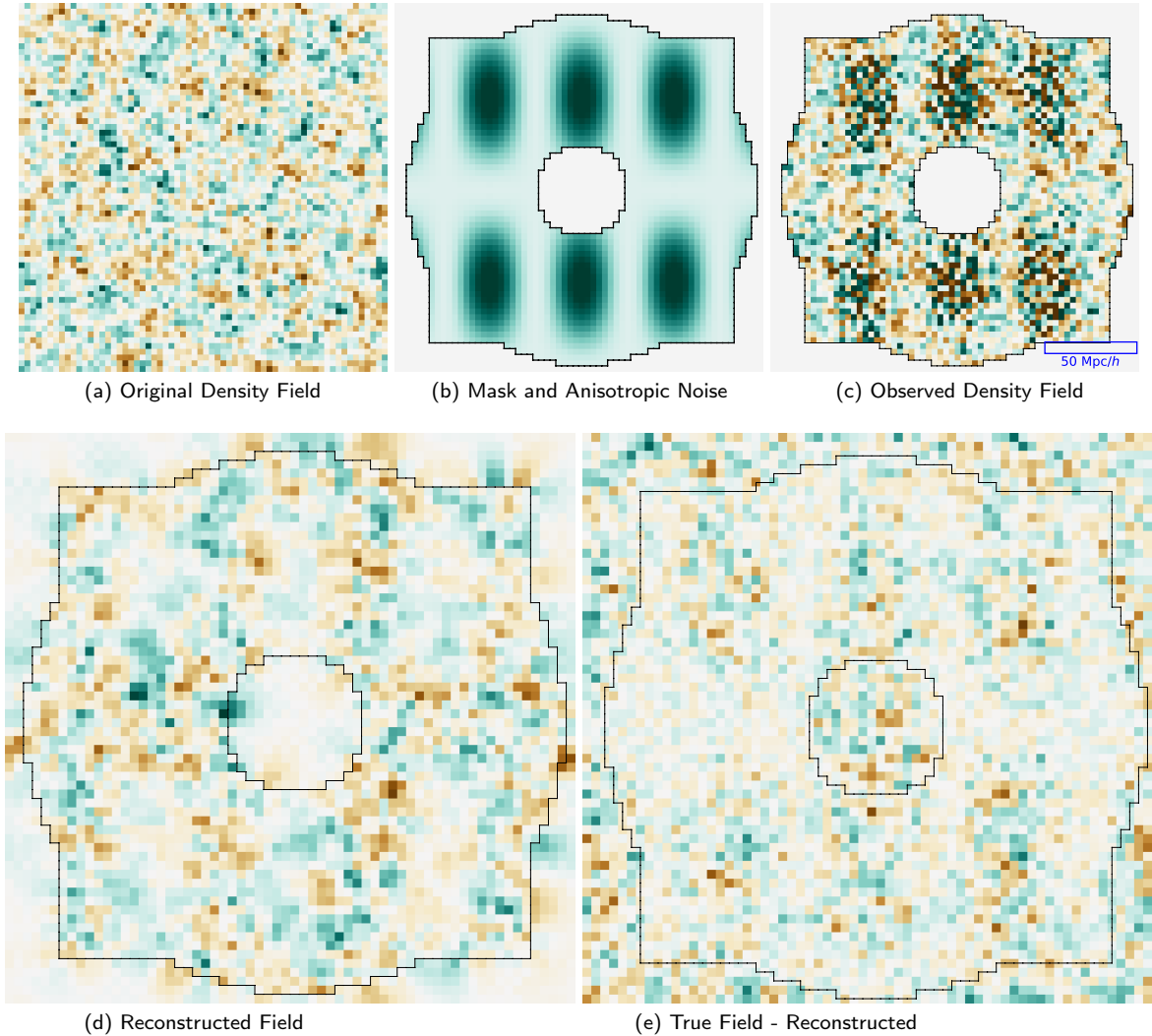


Figure 7: MAP density reconstruction for the 64x64 case.

and the Hessian matrix itself as

$$F_{ll'} = \text{tr}(\mathbf{C}^{-1} \mathbf{Q}_l \mathbf{C}^{-1} \mathbf{Q}_{l'}) = \frac{1}{2} |\boldsymbol{\Pi}_l \mathbf{R}^\dagger \mathbf{C}^{-1} \mathbf{R} \boldsymbol{\Pi}_l|^2. \quad (\text{A.6})$$

Both the Wiener Filter and the optimal power spectrum estimator first weigh the data by the inverse covariance matrix, essentially down weighting modes that either have high measurement error or strong correlation with other measurements (making it provide minimal marginal information).

A.2 Wiener Filtering vs. MAP Projected Density Example

As a numerically exact Wiener filtering is computationally expensive as it requires the direct inversion of a matrix with the square of the number of pixels in the survey, we specialize our comparison to a small 64×64 pixel image.

Using the input power spectrum of Eq. 3.1 we generate a density field shown in Fig 7(a), apply a mask and anisotropic noise shown in Fig 7(b), which results in a mock observation

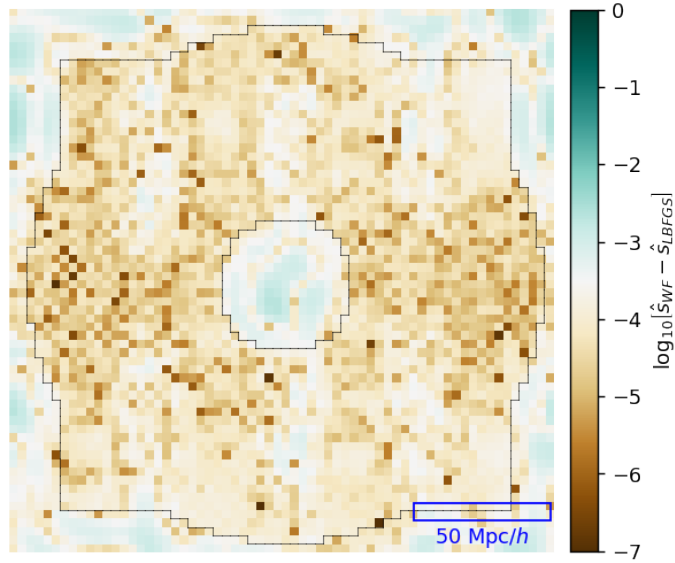


Figure 8: The log absolute magnitude difference of the direct matrix inversion Wiener filter solution and that attained via a MAP method. Note that differences are extremely small throughout the map and are particularly small in the unmasked region.

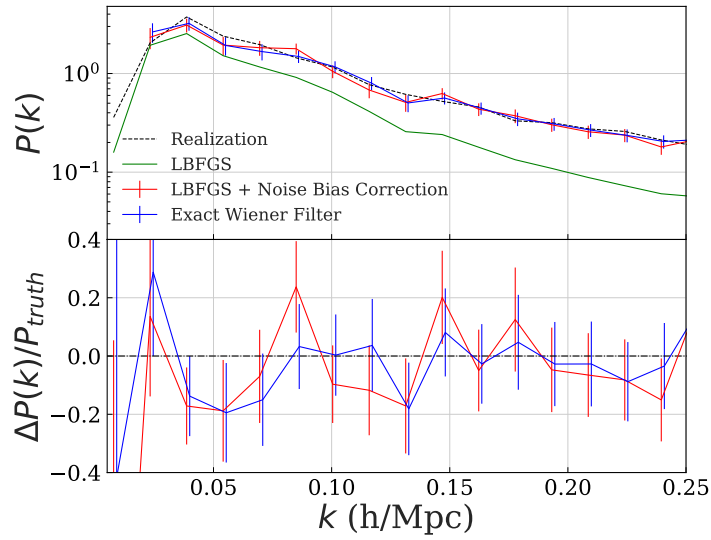


Figure 9: Comparison of the maximum likelihood power spectrum attained from optimization versus that for brute force matrix inversion Wiener filter. Errors are visually identical, and all points k bins are within one standard deviation of each other.

in Fig 7(c). We perform the minimization routine outlined in Sec. 2.2, with the optimized map shown in Fig. 7(d) with residuals shown in Fig 7(e). Visually, the reconstructed field does an excellent job within the mask in the low-noise regions and is even able to reconstruct the larger scale modes right on the border within the masked region. However, as expected, the small scale modes within the high noise regions within the mask are poorly reconstructed since it is impossible to differentiate those modes in real space with the noise.

For this small test case we can compare the optimization result directly against a numerical inversion Wiener filter solution, which we show on the map level in Fig 8. The results match outside the masked region within 10^{-4} , while in the masked region there is a slightly large difference due to the imposition of a convergence criteria in our L-BFGS scheme. As we increase the required precision of the L-BFGS in terms of $\epsilon \equiv \Delta\chi^2$, we asymptotically approach the Wiener filter solution.

Using the formulation in Sec 2.3, we can look at the performance of the technique as a function of scale. In Fourier space we can account for the reduction of small scale power caused by noise and also estimate the Hessian matrix (thereby giving error estimates). We show the power spectrum and error estimates from the optimization technique versus the direct Wiener filtering in Fig 9. Note that the full reconstruction relies on both calculation of noise bias and Hessian matrix. We have compared each of these terms from the optimization method to those calculated via direct matrix inversion to confirm they are equal within the error of the required optimization precision. Also note that we only used one noise realization to estimate the noise bias. In general, the number of noise realizations necessary to appropriately estimate the number of underlying band-powers will depend on both the underlying noise model and the band-powers of interest. In this particular case we found the improvements from including multiple noise realizations minimal as the effect on the overall power-spectrum were sub 1%.

B Convergence Criteria of CMB Reconstruction

An important question to answer is to what the required convergence criteria are for a given algorithm/observable. In general, this will depend on what sort of scales are being probed and what other sources of error exist in the problem. In this section we will consider how changing the convergence criteria, $\epsilon \equiv \Delta\chi^2$, affects the net reconstructed map. We will specialize our analysis to that of the CMB case since it has the largest condition number, and most power on large scales, which will be particularly sensitive to reconstruction within the masked region. A similar analysis with our cosmic shear example will lead to smaller effects.

To demonstrate the convergence properties of our technique we performed a high-accuracy run demanding $\epsilon < 10^{-4}$ as our convergence criteria, as opposed to $\epsilon < 10^{-1}$ for the runs in the main body of the paper. We show these results, as well as the difference with the true field, in Figure 10. Note that very quickly we find the true solution in the unmasked region, but continue to reconstruct the large scale modes in the masked region as the optimization rerouting continues.

We compare our convergence accuracy as a function of scale to the cosmic variance limit in Figure 11. While in practice one wants the error on the reconstruction to be well below this limit, it provides a useful guideline for the necessary accuracy for reconstruction. Note that the properties of this reconstruction are a function primarily of the survey geometry; a hypothetical full sky survey with no masked region and similar noise properties would converge much quicker to the optimal solution. Similarly, a case with smaller masked regions

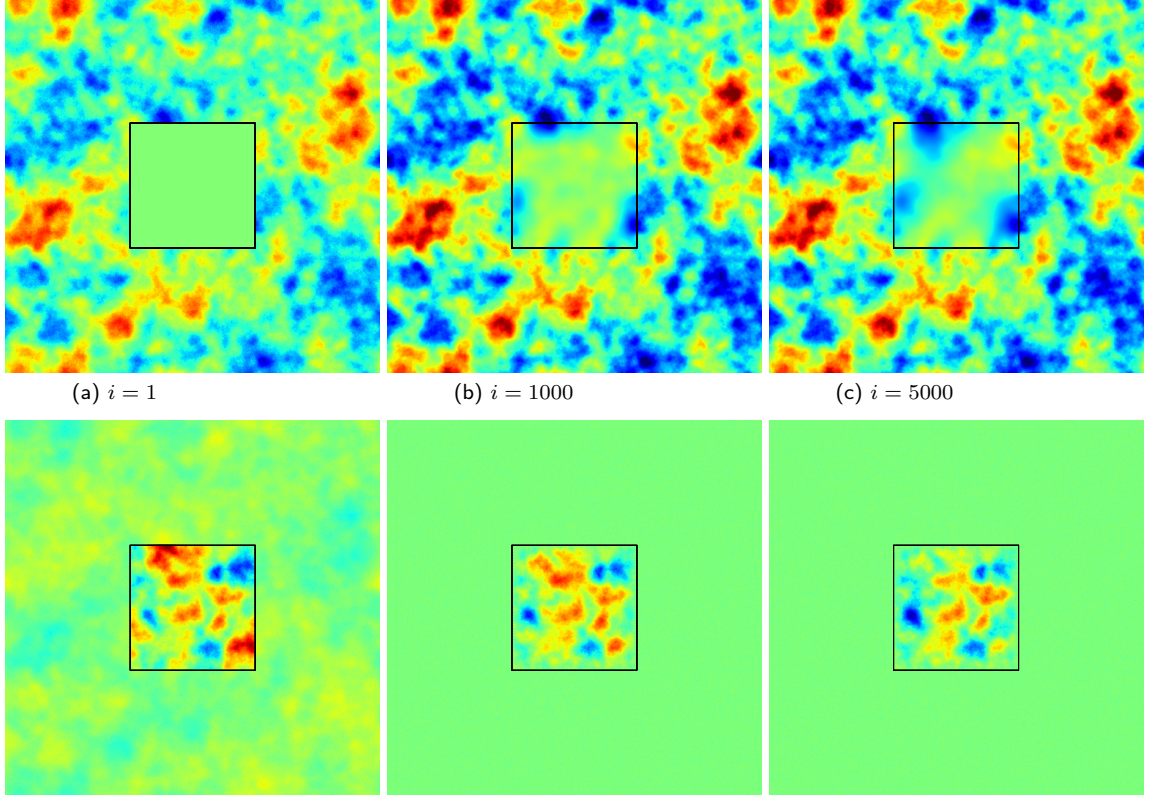


Figure 10: *Top:* Reconstructed density field at given iteration. *Bottom:* Difference of true density field with reconstruction at each iteration. Note that we have used the same mask/noise properties as in Sec 3.2.

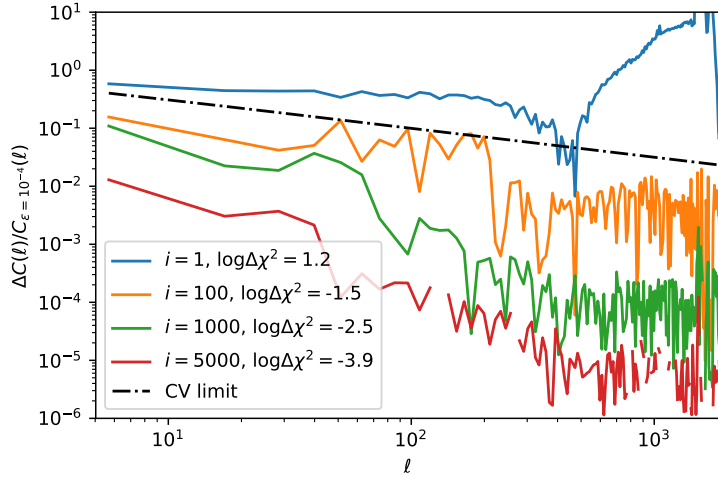


Figure 11: Change in convergence properties as a function of scale. We compare against the high convergence solution ($\epsilon = 10^{-4}$) rather than the true solution as the presence of noise will bias the end power spectra and calculating the noise bias and the Fisher information matrix (Hessian) for each step of the iteration would be computationally expensive.

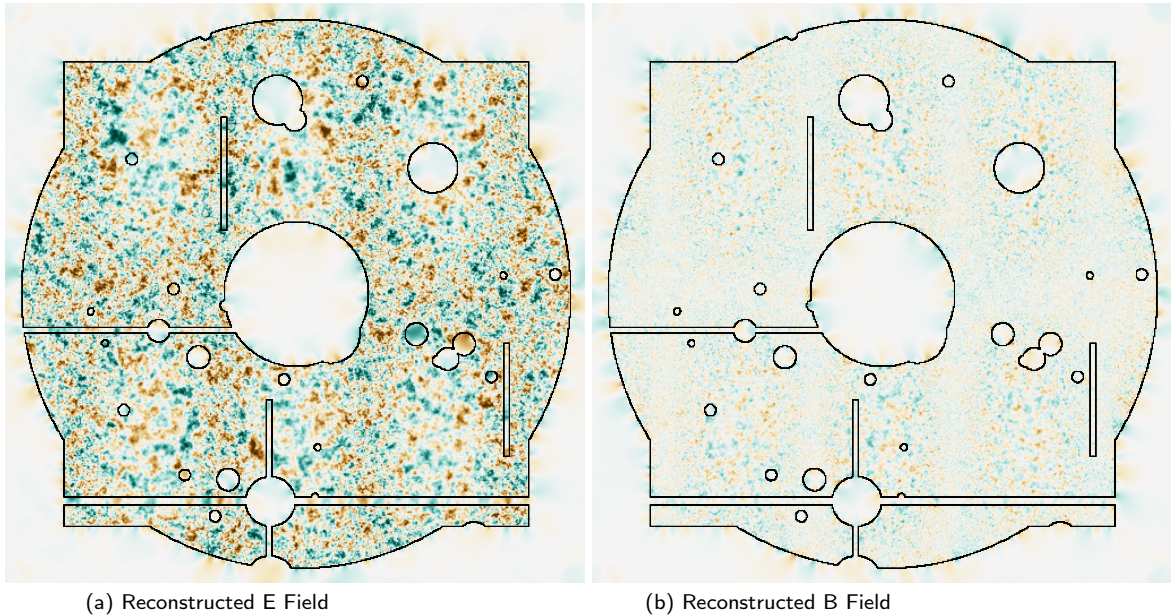


Figure 12: Maximum likelihood E and B potential fields for cosmic shear case. Noise properties and mask are the same as in Section 3.3.

(for example only stellar masking) would find much faster convergence of the large scale modes.

C Joint E & B Cosmic Shear Reconstruction

In the main text we only explored reconstructing the primary (i.e. curl-free) E -mode lensing potential of cosmic shear. However, there are various potential sources of B -mode effects within realistic observed lensing maps, such as instrumental effects, clustering of source galaxies [34], and intrinsic alignments of galaxy shapes [35, 36]. To control for these effects it is useful to perform a joint optimization of both E and B modes from the shear maps. The same tools could also be applied directly to the CMB polarization field from the Q and U maps [28].

The observed shear fields γ_1 and γ_2 can be expressed in terms of the E and B potentials as

$$\begin{bmatrix} \gamma_1 \\ \gamma_2 \end{bmatrix} = \begin{bmatrix} (\partial_x^2 - \partial_y^2) & -2\partial_x\partial_y \\ 2\partial_x\partial_y & (\partial_x^2 - \partial_y^2) \end{bmatrix} \begin{bmatrix} \phi_E \\ \phi_B \end{bmatrix}, \quad (\text{C.1})$$

where we assume flat sky. Our response matrix now takes two signal fields (ϕ_E and ϕ_B) to two data fields (γ_1 and γ_2) and we perform the optimization over the signal fields.

To study the joint reconstruction, we use the same starting E field as in Subsection 3.3, but also induce a B field which has a power spectrum with the same shape as the E field but an amplitude 10^{-5} times smaller. We then do a joint reconstruction of both fields, yielding results shown in Fig 12.

The power spectrum estimation is now slightly more complicated as the Hessian matrix now has EE, BB, as well as EB, BE components to sum over, as shown in Fig 13. The

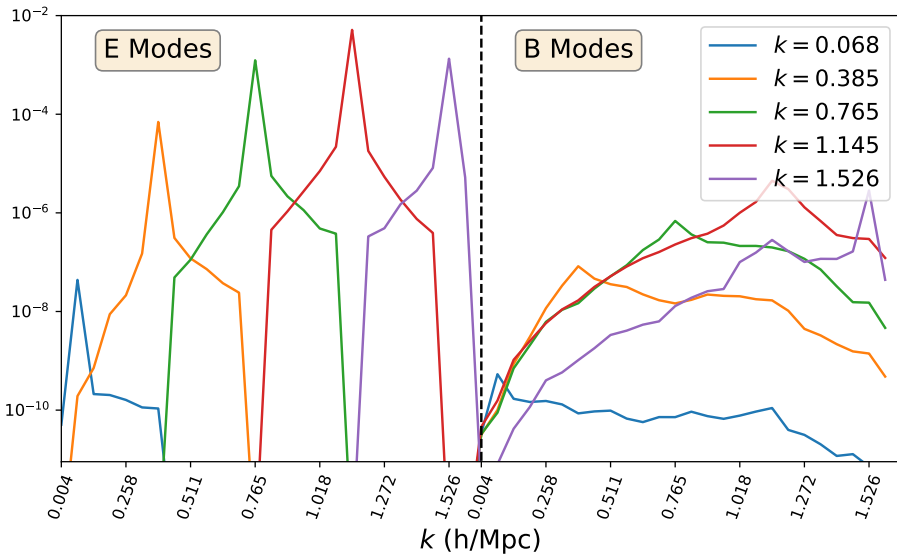
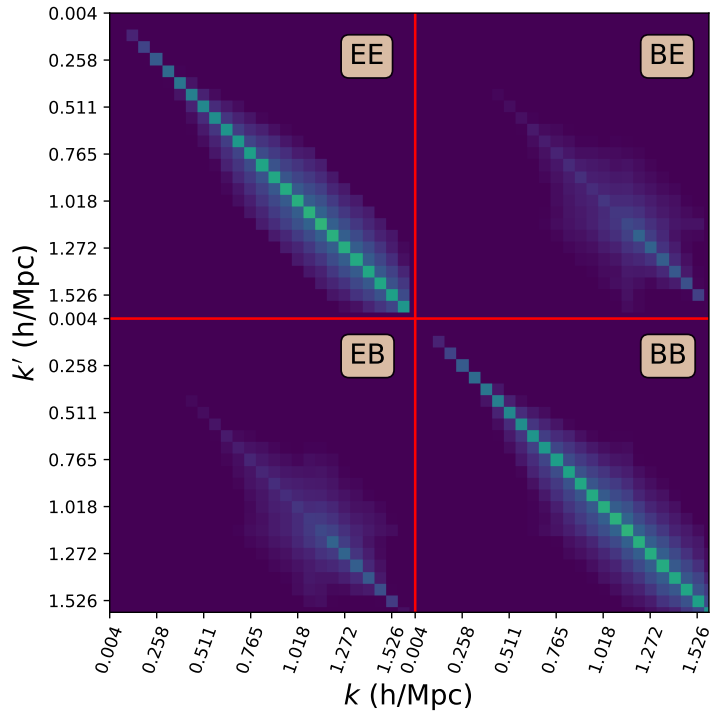


Figure 13: *Top:* Full two dimensional Fisher matrix for the cosmic shear E/B joint reconstruction case. The matrix can be viewed as 4 blocks, with EE and BB the response of each type of mode to itself and the BE and EB reflecting the leakage between the modes induced by the survey geometry. *Bottom:* Vertical cuts of the Fisher matrix. Note that to reduce numerical noise in the final reconstruction we have zeroed out terms in the EE/BB blocks far from the diagonal.

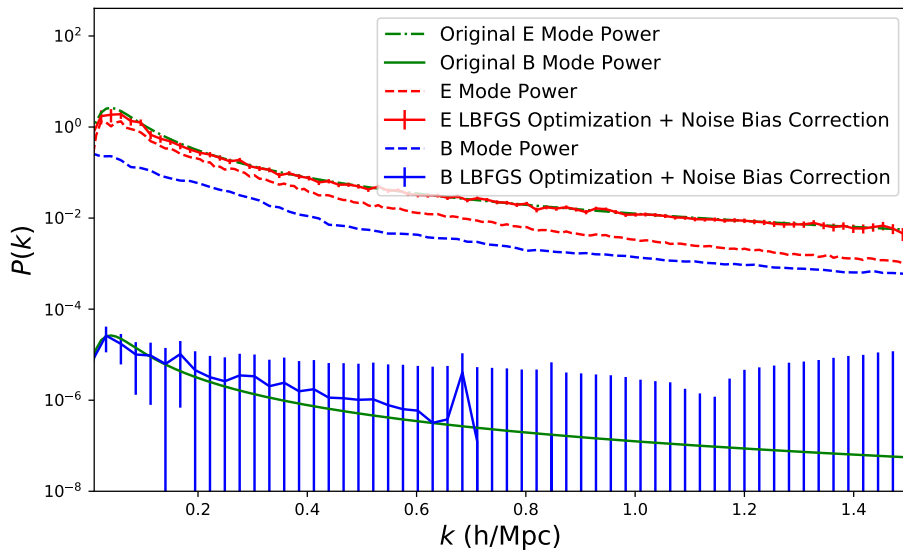


Figure 14: Reconstruction of the E and B power spectrum from mock observations using the maximum likelihood technique described in this work. Green lines indicate the original E/B power of the signal maps. The dashed red and blue lines indicate the power from the LBFSG optimized maps of E and B power respectively, while the solid lines indicate their MAP power spectra.

EB/BE components represent leakage between the channels, which in this case is dominated by E power leaking into B. We show this power spectrum reconstruction in Figure 14. This is visually apparent in the reconstruction as we find an over-abundance of B power in the reconstructed map, which then gets down-weighted when this leakage is accounted for. In addition, as the B mode power is dominated by noise, it is difficult to accurately reconstruct its power from this one mock observation.

Alternatively, rather than perform a full Fisher-like analysis for the B-mode power one could instead perform multiple realizations of the B-mode leakage and average them together to form a “leakage bias” in analogous way as for the noise terms. This would have the possible advantage of requiring an additional optimization for each realization of the B-mode power, rather than an optimization for each mode of injected power as for the full Fisher analysis. If one is interested in studying many modes at once, treating the B-modes like noise bias would be computationally expedient.

References

- [1] N. Wiener, *Extrapolation, interpolation, and smoothing of stationary time series: with engineering applications*, .
- [2] G. B. Rybicki and W. H. Press, *Interpolation, realization, and reconstruction of noisy, irregularly sampled data*, *ApJ* **398** (Oct., 1992) 169–176.
- [3] K. B. Fisher, O. Lahav, Y. Hoffman, D. Lynden-Bell, and S. Zaroubi, *Wiener reconstruction of density, velocity and potential fields from all-sky galaxy redshift surveys*, *MNRAS* **272** (Feb., 1995) 885–908, [[astro-ph/9406009](#)].

- [4] F. S. Kitaura and T. A. Enßlin, *Bayesian reconstruction of the cosmological large-scale structure: methodology, inverse algorithms and numerical optimization*, *MNRAS* **389** (Sept., 2008) 497–544, [[arXiv:0705.0429](#)].
- [5] E. F. Bunn, Y. Hoffman, and J. Silk, *The Wiener-filtered COBE DMR Data and Predictions for the Tenerife Experiment*, *ApJ* **464** (June, 1996) 1, [[astro-ph/9509045](#)].
- [6] M. Tegmark, A. de Oliveira-Costa, and A. J. Hamilton, *High resolution foreground cleaned CMB map from WMAP*, *PRD* **68** (Dec., 2003) 123523, [[astro-ph/0302496](#)].
- [7] E. Komatsu, D. N. Spergel, and B. D. Wandelt, *Measuring Primordial Non-Gaussianity in the Cosmic Microwave Background*, *ApJ* **634** (Nov., 2005) 14–19, [[astro-ph/0305189](#)].
- [8] F. Elsner and B. D. Wandelt, *Efficient Wiener filtering without preconditioning*, *A&A* **549** (Jan., 2013) A111, [[arXiv:1210.4931](#)].
- [9] J. Alsing, A. Heavens, A. H. Jaffe, A. Kiessling, B. Wandelt, and T. Hoffmann, *Hierarchical cosmic shear power spectrum inference*, *MNRAS* **455** (Feb., 2016) 4452–4466, [[arXiv:1505.07840](#)].
- [10] D. Kodi Ramanah, G. Lavaux, and B. D. Wandelt, *Wiener filter reloaded: fast signal reconstruction without preconditioning*, *MNRAS* **468** (June, 2017) 1782–1793, [[arXiv:1702.08852](#)].
- [11] J. Papez, L. Grigori, and R. Stompor, *Solving linear equations with messenger-field and conjugate gradients techniques - an application to CMB data analysis*, *ArXiv e-prints* (Mar., 2018) [[arXiv:1803.03462](#)].
- [12] U. Seljak, *Cosmography and Power Spectrum Estimation: A Unified Approach*, *ApJ* **503** (Aug., 1998) 492–501, [[astro-ph/9710269](#)].
- [13] J. Alsing, A. Heavens, and A. H. Jaffe, *Cosmological parameters, shear maps and power spectra from CFHTLenS using Bayesian hierarchical inference*, *MNRAS* **466** (Apr., 2017) 3272–3292, [[arXiv:1607.00008](#)].
- [14] P. Simon, A. N. Taylor, and J. Hartlap, *Unfolding the matter distribution using three-dimensional weak gravitational lensing*, *MNRAS* **399** (Oct., 2009) 48–68, [[arXiv:0907.0016](#)].
- [15] U. Seljak, G. Aslanyan, Y. Feng, and C. Modi, *Towards optimal extraction of cosmological information from nonlinear data*, *ArXiv e-prints* (June, 2017) [[arXiv:1706.06645](#)].
- [16] J. R. Bond, A. H. Jaffe, and L. Knox, *Estimating the power spectrum of the cosmic microwave background*, *PRD* **57** (Feb., 1998) 2117–2137, [[astro-ph/9708203](#)].
- [17] M. Tegmark, *How to measure CMB power spectra without losing information*, *PRD* **55** (May, 1997) 5895–5907, [[astro-ph/9611174](#)].
- [18] Planck Collaboration, N. Aghanim, M. Arnaud, M. Ashdown, J. Aumont, C. Baccigalupi, A. J. Banday, R. B. Barreiro, J. G. Bartlett, N. Bartolo, and et al., *Planck 2015 results. XI. CMB power spectra, likelihoods, and robustness of parameters*, *A&A* **594** (Sept., 2016) A11, [[arXiv:1507.02704](#)].
- [19] Planck Collaboration, P. A. R. Ade, N. Aghanim, M. Arnaud, M. Ashdown, J. Aumont, C. Baccigalupi, A. J. Banday, R. B. Barreiro, J. G. Bartlett, and et al., *Planck 2015 results. XIII. Cosmological parameters*, *A&A* **594** (Sept., 2016) A13, [[arXiv:1502.01589](#)].
- [20] K. M. Górski, E. Hivon, A. J. Banday, B. D. Wandelt, F. K. Hansen, M. Reinecke, and M. Bartelmann, *HEALPix: A Framework for High-Resolution Discretization and Fast Analysis of Data Distributed on the Sphere*, *ApJ* **622** (Apr., 2005) 759–771, [[astro-ph/0409513](#)].
- [21] L. Van Waerbeke, Y. Mellier, M. Radovich, E. Bertin, M. Dantel-Fort, H. J. McCracken, O. Le Fèvre, S. Foucaud, J.-C. Cuillandre, T. Erben, B. Jain, P. Schneider, F. Bernardeau, and

- B. Fort, *Cosmic shear statistics and cosmology*, *A&A* **374** (Aug., 2001) 757–769, [[astro-ph/0101511](#)].
- [22] M. Bartelmann and P. Schneider, *Weak gravitational lensing*, *PhysRep* **340** (Jan., 2001) 291–472, [[astro-ph/9912508](#)].
- [23] B. Jain and U. Seljak, *Cosmological Model Predictions for Weak Lensing: Linear and Nonlinear Regimes*, *ApJ* **484** (July, 1997) 560–573, [[astro-ph/9611077](#)].
- [24] N. Padmanabhan, U. Seljak, and U. L. Pen, *Mining weak lensing surveys.*, *New Astronomy* **8** (2003) 581–603, [[astro-ph/0210478](#)].
- [25] V. Böhm, S. Hilbert, M. Greiner, and T. A. Enßlin, *Bayesian weak lensing tomography: Reconstructing the 3D large-scale distribution of matter with a lognormal prior*, *PRD* **96** (Dec., 2017) 123510, [[arXiv:1701.01886](#)].
- [26] N. Kaiser, G. Squires, and T. Broadhurst, *A Method for Weak Lensing Observations*, *ApJ* **449** (Aug., 1995) 460–+.
- [27] N. Jeffrey, F. B. Abdalla, O. Lahav, F. Lanusse, J.-L. Starck, A. Leonard, D. Kirk, C. Chang, E. Baxter, T. Kacprzak, S. Seitz, V. Vikram, L. Whiteway, T. M. C. Abbott, S. Allam, S. Avila, E. Bertin, D. Brooks, A. Carnero Rosell, M. Carrasco Kind, J. Carretero, F. J. Castander, M. Crocce, C. E. Cunha, C. B. D’Andrea, L. N. da Costa, C. Davis, J. De Vicente, S. Desai, P. Doel, T. F. Eifler, A. E. Evrard, B. Flaugher, P. Fosalba, J. Frieman, J. Garcia-Bellido, D. W. Gerdes, D. Gruen, R. A. Gruendl, J. Gschwend, G. Gutierrez, W. G. Hartley, K. Honscheid, B. Hoyle, D. J. James, M. Jarvis, K. Kuehn, M. Lima, H. Lin, M. March, P. Melchior, F. Menanteau, R. Miquel, A. A. Plazas, K. Reil, A. Roodman, E. Sanchez, V. Scarpine, M. Schubnell, I. Sevilla-Noarbe, M. Smith, M. Soares-Santos, F. Sobreira, E. Suchyta, M. E. C. Swanson, G. Tarle, D. Thomas, and A. R. Walker, *Improving Weak Lensing Mass Map Reconstructions using Gaussian and Sparsity Priors: Application to DES SV*, *ArXiv e-prints* (Jan., 2018) [[arXiv:1801.08945](#)].
- [28] C. M. Hirata and U. Seljak, *Reconstruction of lensing from the cosmic microwave background polarization*, *PRD* **68** (Oct., 2003) 083002, [[astro-ph/0306354](#)].
- [29] J. Carron and A. Lewis, *Maximum a posteriori CMB lensing reconstruction*, *PRD* **96** (Sept., 2017) 063510, [[arXiv:1704.08230](#)].
- [30] W. Hu and T. Okamoto, *Mass Reconstruction with Cosmic Microwave Background Polarization*, *ApJ* **574** (Aug., 2002) 566–574, [[astro-ph/0111606](#)].
- [31] B. Horowitz, S. Ferraro, and B. D. Sherwin, *Reconstructing Small Scale Lenses from the Cosmic Microwave Background*, *ArXiv e-prints* (Oct., 2017) [[arXiv:1710.10236](#)].
- [32] R. M. Szepietowski, D. J. Bacon, J. P. Dietrich, M. Busha, R. Wechsler, and P. Melchior, *Density mapping with weak lensing and phase information*, *MNRAS* **440** (May, 2014) 2191–2200, [[arXiv:1306.5324](#)].
- [33] P. Simon, *Improving three-dimensional mass mapping with weak gravitational lensing using galaxy clustering*, *A&A* **560** (Dec., 2013) A33, [[arXiv:1203.6205](#)].
- [34] P. Schneider, L. van Waerbeke, and Y. Mellier, *B-modes in cosmic shear from source redshift clustering*, *A&A* **389** (July, 2002) 729–741, [[astro-ph/0112441](#)].
- [35] C. M. Hirata and U. Seljak, *Intrinsic alignment-lensing interference as a contaminant of cosmic shear*, *PRD* **70** (Sept., 2004) 063526, [[astro-ph/0406275](#)].
- [36] M. A. Troxel and M. Ishak, *The intrinsic alignment of galaxies and its impact on weak gravitational lensing in an era of precision cosmology*, *PhysRep* **558** (Feb., 2015) 1–59, [[arXiv:1407.6990](#)].